Picosecond Pulsed Laser Ablation of Liquid Covered Stainless Steel: Effect of Liquid Layer Thickness on Ablation Efficiency

Sietse van der Linden[1], Rob Hagmeijer[2] and Gert-willem Römer[1]

[1] *Chair of Laser Processing, Department of Mechanics of Solids, Surfaces & Systems (MS³), Faculty of Engineering Technology, University of Twente, P.O. Box 217, 7500 AE, Enschede, The Netherlands*
E-mail: s.vanderlinden@utwente.nl
[2] *Chair of Engineering Fluid Dynamics, Department of Thermal and Fluid Engineering, Faculty of Engineering Technology, University of Twente, P.O. Box 217, 7500 AE, Enschede, The Netherlands*

Under liquid laser ablation is a material removal technique in which a focused laser beam passes through a liquid layer on top of the surface of a sample to be processed. When compared to laser ablation without a liquid layer, material (re)deposition around ablated regions is decreased. In addition, the ablation efficiency of the process, in terms of the amount of material removed per pulse, can be optimized by careful variation of the height of the liquid layer: a liquid layer height variation as small as a few tenth of millimeters already has a measurable effect on the amount of ablated material. In studies reported in existing literature, the required liquid layer height is typically realized by pouring a pre-defined amount of liquid on top of the sample surface. Surface tension, however, causes the air-liquid interface at the boundaries of the domain to deviate from the planar interface away from the boundaries, which affects the accuracy with which the liquid layer height can be determined. To the best of our knowledge, these accuracy issues have not been studied in previous research. Therefore, an experimental set-up is proposed which circumvents the issues of a curved free surface. Next, a 7 picosecond pulsed laser source ($M^2 \leq 1.3$) at a wavelength of 515nm was employed at a repetition rate of 1 kHz to study the efficiency of laser ablation of stainless steel for a range of liquid layer heights. Our findings provide a more detailed quantification of crater depth as a function of liquid layer height than is available through existing literature.

DOI: 10.2961/jlmn.2019.01.0018
Keywords: laser, ablation, stainless steel, picosecond, liquid, distilled water

Introduction

Under liquid laser ablation is a material removal technique in which a focused laser beam passes through a liquid layer on top of the surface of a sample to be processed. Advantages of this method over conventional in air laser processing include a reduction of debris around the ablated region [1] and a decrease of heat affected zone [2]. Additionally, under liquid laser ablation has been studied to create surface textures by varying the type of liquids involved in the process [3,4]. Past research found that the liquid increases the volume of material removed per laser pulse when compared to ablation in ambient air, using the same laser parameters [5,6]. In particular, Zhu et al [6], found that ablated volume is a highly sensitive function of liquid layer height, with changes as small as 0.1 mm in liquid layer height causing noticeable effects on the amount of sample volume removed per laser pulse. To the best of the authors' knowledge, liquid layer height is not controlled down to this length scale in existing literature [7–9]. Therefore, this paper studies the influence of the liquid layer height on ablation results in terms of ablated crater morphology and material removal rate. To that end, this paper presents results obtained by a setup that more accurately controls the liquid layer height than in existing laser set-ups.

1. Experimental set-up

A 7 ps pulsed Yb:Yag laser source (TruMicro5050 of Trumpf, Germany) with a fundamental wavelength of 1030 nm was frequency doubled to 515 nm using a second harmonic generator (SHG). The beam quality of this source equals $M^2<1.3$. The pulse frequency was set to 1 kHz to reduce laser-beam interaction with a bubble formed by an earlier laser pulse. A more thorough analysis of these bubbles is presented in section 3. A combination of a $\lambda/2$ plate and a polarizing beam splitter was employed to attenuate the laser beam. The beam was then guided through the SHG into a plano-convex lens (LA1509 of Thorlabs, Germany) with a focal length of 100 mm. The plano-convex lens ensured that the laser light was directed at the side-wall of an optically transparent and watertight box, see Fig. 1 and Fig. 2. The focal spot diameter after passing through the optically transparent box was determined to be approximately 26 μm by means of the well-known D^2-method [10–13]. The optically transparent walls consist of four 4 mm thick 50 by 50 mm square silica glass plates and a base plate of aluminum. The glass plates were coated with a visible light anti-reflective coating. The box was mounted to a xyz-stage (RB13D/M of Thorlabs, Germany) to allow accurate positioning of the box with respect to the incident laser beam. Two steel gauge blocks with a thickness defined with an accuracy better than

1 μm were mounted to the inside of the wall facing the incoming laser beam using magnets placed on the outside of the silica glass, see Fig. 2. Stainless steel 304 samples (plates) of approximately 20 by 20 mm were used for the performed experiments. These samples were embedded in an epoxy, after which they were grinded and subsequently polished to obtain a surface roughness of R_a 0.16 µm. Then, a sample was placed inside the transparent box prior to filling it with distilled water. To maintain a fixed distance between the fused silica wall and the surface of the sample, the sample was then pressed against the gauge blocks by placing magnets on the backend of the epoxy embedded sample. Due to the sizing accuracy of the spacers, this method guarantees a very precisely defined space between the inside of the silica glass wall and the surface of the sample. Next, distilled water was poured into the box. After having filled the box, the gauge blocks ensure a fixed liquid layer thickness through which the laser beam will pass. Note that the laser beam is not propagating vertically and imping on the sample surface from the top, but, the laser beam is horizontally impinging the surface of the sample. The liquid layer thickness could (and was) altered in the experiments by using pairs of gauge blocks with different thicknesses. Benefits of ablating in this manner rather than by aiming the laser at the free surface of the liquid onto the sample is the absence of free surface waves. The latter would deflect and/or scatter the laser beam. Additionally, in this setup, bubbles formed during the processing will drift upward and away from the laser-material interaction zone due to buoyancy. Power measurements were performed using a power meter and a photodiode (PM100A of Thorlabs, Germany) and a power sensor (S130VC of Thorlabs, Germany).

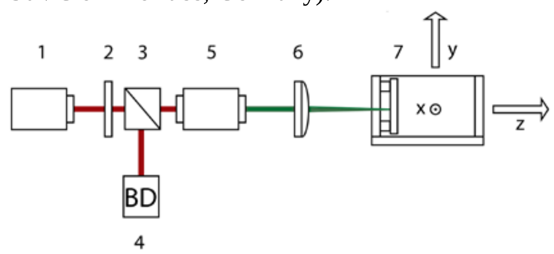

Fig. 1 Schematic of the experimental set-up. Numbers denote: 1: Yb:YAG laser source, 2: 1/2λ plate, 3: polarizing beam splitter, 4: beam dump, 5: second harmonic generator, 6: plano-convex lens (f = 100 mm), 7: transparent box on xyz-stage.

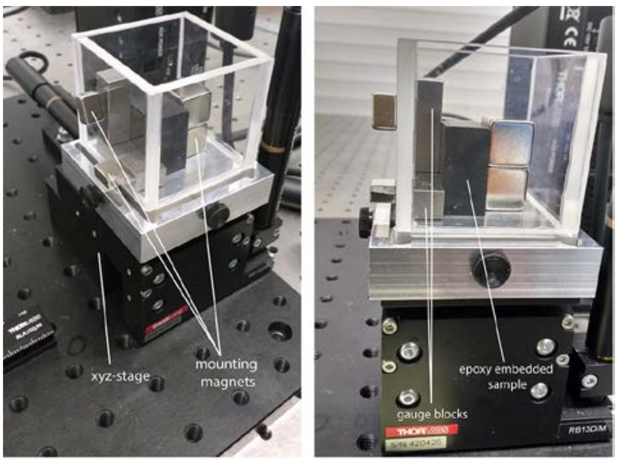

Fig. 2 Photographs of transparent box (without liquid) from two different angles.

2. Method

First, the focus position relative to the surface of the sample was determined in ambient air by mounting a sample on the gauge blocks without filling the box with distilled water. Next, in order to study the effect of laser energy on the resulting ablated craters, three different pulse energy levels were chosen, namely 0.5, 1.0, and 2.2 µJ respectively. These pulse energies were determined by placing the detector between the plano-convex lens and the optically transparent box. To determine the actual pulse energies deposited onto the sample, reflections at the different media interfaces the laser passes through must be taken into account. A method to do so was proposed in literature [14] and was employed to determine the pulse energies at the surface of the sample. The method is briefly discussed below. Here we denote the pulse energies in front of the optically transparent box as $E_{p,lens}$. The pulse energy on the sample in ambient air and ambient water respectively may then be determined by

$$E_{p,air} = E_{p,lens} \cdot T_{air}, \tag{1}$$
$$E_{p,water} = E_{p,lens} \cdot T_{water}, \tag{2}$$

in which T_{air} and T_{water} are the transmission values compensated for Fressnel reflection at the media interfaces the laser passes through, which are defined as

$$T_{air} = T_{air/silica} \cdot T_{silica/air} \cdot T_{air/ss304}, \tag{3}$$
$$T_{water} = T_{air/silica} \cdot T_{silica/water} \cdot T_{water/ss304}, \tag{4}$$

in which the different T values are transmissions through the interfaces denoted by the subscripts. Transmissions from interface 1 to 2 can be computed by

$$T_{1/2} = 1 - R_{1/2}, \tag{5}$$

in which $R_{1/2}$ denotes the reflection coefficient for the interface between media 1 and 2. This value can then be computed using

$$R_{1/2} = \left|\frac{\tilde{n}_1 - \tilde{n}_2}{\tilde{n}_1 + \tilde{n}_2}\right|^2, \tag{6}$$

with $\tilde{n}$ defined as the complex refractive index of a medium

$$\tilde{n} = n + ik, \tag{7}$$

in which n is the refractive index and k the extinction coefficient of a medium. The complex refractive indexes for all relevant materials in this paper are given in table 1. We determined the optical constants of 304 stainless steel by ellipsometry (Woollam M200UI of Woollam, United States of America). The calculated transmission values for all interfaces are summarized in Table 2.

Table 1 Complex refractive index of different materials. Note that the index of stainless steel 304 was determined by ellipsometry

Material	n	k	Reference
Air	1.000	0	[15]
Silica	1.462	0	[16,17]
Water	1.330	0	[18]
Stainless steel 304	2.000	3.471	this work

Table 2 Total calculated transmission values for ablation in ambient air and in ambient water and transmission values for medium interfaces.

Transmission	Value
T_{air}	0.354
T_{water}	0.443
$T_{air/silica}$	0.965
$T_{silica/air}$	0.965
$T_{air/ss304}$	0.380
$T_{silica/water}$	0.998
$T_{water/ss304}$	0.460

Based on the transmission values, the pulse energies at the sample surface were determined to equal 0.18, 0.35 and 0.78 µJ for ablation in ambient air and 0.22, 0.44 and 0.97 µJ for ablation in ambient water. From this point onward, all references with respect to pulse energies will be made with respect to the pulse energies at the sample surface rather than the values measured in between the plano-convex lens and the optically transparent box. The number of consecutive laser pulses impinging on the surface of the sample were chosen as N =1, 2, 3 and 5. This yielded a total of 12 different laser processing conditions. This procedure was then repeated for 10 different liquid layer thicknesses ranging from 1 to 10 mm with 1 mm increments. It should be noted that the liquid layer induces a focus shift when compared to the focus position in ambient air, which may be compensated for by moving the transparent box in opposite direction of the incident laser beam over a distance of [19], see also Fig. 3:

$$\Delta H = H_L(1 - 1/n) \tag{8}$$

Where H_L denotes the liquid layer height and n = 1.33 is the refractive index of distilled water. A schematic illustrating the different variables is provided in Fig. 3.

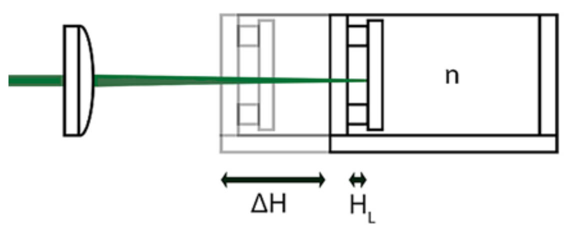

Fig. 3 Schematic (top view) depicting the focus shift ΔH required to acquire focus under a liquid layer of thickness H_L. Variables/symbols are defined w.r.t. equation (1). The faded image denotes focus in air, the non-faded picture denotes focus under a liquid layer. Note that the focus shift is exaggerated.

3. Analysis tools

Analysis of the ablated craters was performed using a Scanning Electron Microscope (SEM, JSM-7200F of JEOL, Japan), a Confocal Laser Scanning Microscope (CLSM, VK-9710 of Keyence, Japan) and an Atomic Force Microscope (AFM, XE-100 of Park Systems, South Korea). All three measurement systems were used to obtain insight into crater morphologies.

4. Results & discussion

Experiments were performed for both ambient air and ambient distilled liquid conditions using the laser parameters as described in section 2.

4.1 SEM images

The SEM micrographs in Fig. 4 provide an overview of ablated craters obtained at different processing conditions in ambient air. No discernable surface modification was found for single pulse ablation at 0.18 μJ. Typical results for similar laser parameters under a 2 mm distilled water layer are shown in Fig. 5. In ambient air, the single pulse craters are covered by spherically shaped structures presumably created due to melting of the surface. As the pulse energy increases, the melt like structure in the center of the crater becomes more pronounced. Similar to earlier work, ripple structures may be identified at the outer edges of the craters [20]. For all craters in ambient air (Fig. 4), it is clear that the crater is not entirely circular, but slightly elliptic, presumably due to optical aberrations introduced by the lens. In ambient water (Fig. 5), the single pulse craters are characterized by splash like phenomena on the crater surface. As the number of pulse energies increases, these splashes occur more frequently and have larger dimensions. For multiple pulsed craters in ambient water, ripple like fringes can be observed at the outer edges of the craters. Specifically for N = 5, E_p = 0.22 µJ and N = 5, E_p = 0.44 µJ, ring like structures form in the vicinity of the craters (see Fig. 5). Comparing the in air and under liquid ablated craters shows that the crater diameter of under liquid created craters is smaller than their in air counter parts.

To compare the craters in fig. 4 and fig. 5, the ablation crater diameters d_{air} and d_{water} for the craters in fig. 4 were measured and compared to the corresponding craters in fig. 5 to obtain the diameter ratio: $r_{air/water} = d_{air}/d_{water}$. This ratio was then averaged over the number of craters to yield an average diameter ratio of approximately 1.31. To find an explanation for this difference, the D^2 method was used on both the in air and under water ablated craters in order to find the laser spot size on the sample. Laser spot sizes were computed for 2, 3 and 5 consecutive pulses in ambient air, after which the average of the 3 diameters was assumed to be the spot size for ambient air. A similar approach was maintained for 1, 2, 3 and 5 consecutive pulses for the under liquid experiments. This method yielded a spot diameter of 21.8 µm in air and 11.7 µm under water. This indicates the spot size is altered quite drastically by the presence of the liquid which would account for the large crater difference between the two used ambients. Only a limited number of craters could be used for this analysis, creating very large 95% confidence bounds (0.0058 to 0.043 mm for air experiments and 0 to 0.0298 mm for under water experiments). Given this large spread, it is difficult to address the crater diameter difference properly. If the beam waist under water is indeed much smaller than in ambient air, this could been caused by non-linear optical effects occurring in the water. Such effects have been described in literature before for femtosecond pulsed lasers on silicon [21]. Using the pulse energies measured in front of the optically transparent box as an upper limit for peak intensities and power yields $0.31 \cdot 10^6$ W and $7.31 \cdot 10^{10}$ W/cm^2 respectively. These values are significantly lower than the peak intensities and powers required for the non-linear effects to occur [21]. It therefore does not seem likely non-linear effects cause the laser spot diameter to change significantly when changing the ambient environment from air to water. Using the computed spot diameters, peak fluences F_0 were determined for all craters. These values may be found in all images depicting craters.

4.2 Confocal images

Fig. 6 and Fig. 7 show CLSM measurements of the craters marked by a red rectangle in Fig. 4 and Fig. 5. Both top view height profiles (left graphs) and cross sections of the measurements (right graphs) are shown in these figures. The edges of the craters in these CLSM graphs were determined manually and are indicated in both graphs by red crosses. The zero line is the reference height of the average unablated sample surface. Notice that craters produced in air show almost no discernible depth for all but the last CLSM graph. That is, the height of the surface profile of craters produced in air are close to the resolution of the CLSM. Only for the maximum number of pulses and pulse energy, N = 5 and E_p = 0.78 μJ a properly defined crater is formed with a maximum depth of approximately 0.5 μm. In contrast, depth profiles are larger for craters produced under a 2 mm distilled water layer, as maximum depth varies between approximately 0.2 and 0.6 μm. As mentioned, the depth profile is barely discernable for low pulse numbers and energies in ambient air, while for ambient water a crater may be distinguished even for N =1 and E_p = 0.44 μJ. Comparing the last graphs in Fig. 6 and Fig. 7 in terms of maximum crater depth, the difference in maximum crater depth seems to be less significant. This seems to hint that the influence of the liquid on maximum crater depth is dominant for the conditions of the first three CLSM graphs in Fig. 6 and Fig. 7, whereas this influence is of less importance for N = 5 and the highest pulse energies. Adequate conclusions on crater dimensions are difficult to draw however, as the CLSM resolution relative to the crater depth limits the reliability of the graphs. Additionally, it is unclear whether the peak like structures present in the last graph of Fig. 7 originate from the actual surface area of the crater or whether they are a result of the CLSM's inability to track the crater surface area.

4.3 Arc-like surface structures

From the SEM and the CLSM analysis, arc like surface structures were observed in the vicinity of craters produced under the liquid layer, see Fig. 8. These circular structures were found only to occur after 2 or more consecutive laser pulses. And these structures were found to occur only when processing under a liquid layer. Arcs did not seem to have a systematic orientation with respect to craters; some were found to extend outward of the crater in what seems to be random directions, while others overlapped the crater as seen in the lowest micrograph of Fig. 8. Additionally, arc formation seemed independent of the location of the crater on the sample. Roughly 5 different categories of arcs could be distinguished, depending on their location relative to the crater (see Fig. 8):

1. Circular arcs oriented in a half circle directly around the ablated crater, see the top left crater in Fig. 8.
2. Circular arcs oriented in a full circle around the ablation crater, sometimes extending into the ablation crater itself, see the top right crater in Fig. 8.
3. Intersecting arcs with two different radii centers, see the middle left crater in Fig. 8.
4. Circular arcs extending over a large distance outside of the ablation zone, see the middle right crater in Fig. 8.
5. Circular arcs largely confined to the ablation crater area with a radius center eccentric with respect to the crater, see the bottom left crater in Fig. 8.

The arcs were observed for craters created under various different liquid layer heights and only seem to be created when two or more pulses are used to ablate a crater. No comparable structures were observed for the in air ablated craters. The latter indicates that the arcs are a liquid related phenomenon. The peak-to-peak distance (periodicity) of the arcs decreases as the distance to the center of the arc radius increases. If λ is the wavelength of the laser light used to ablate the sample, then periodicity of the ripples ranges between approximately 1/2λ and λ based on the SEM images in Fig. 8.

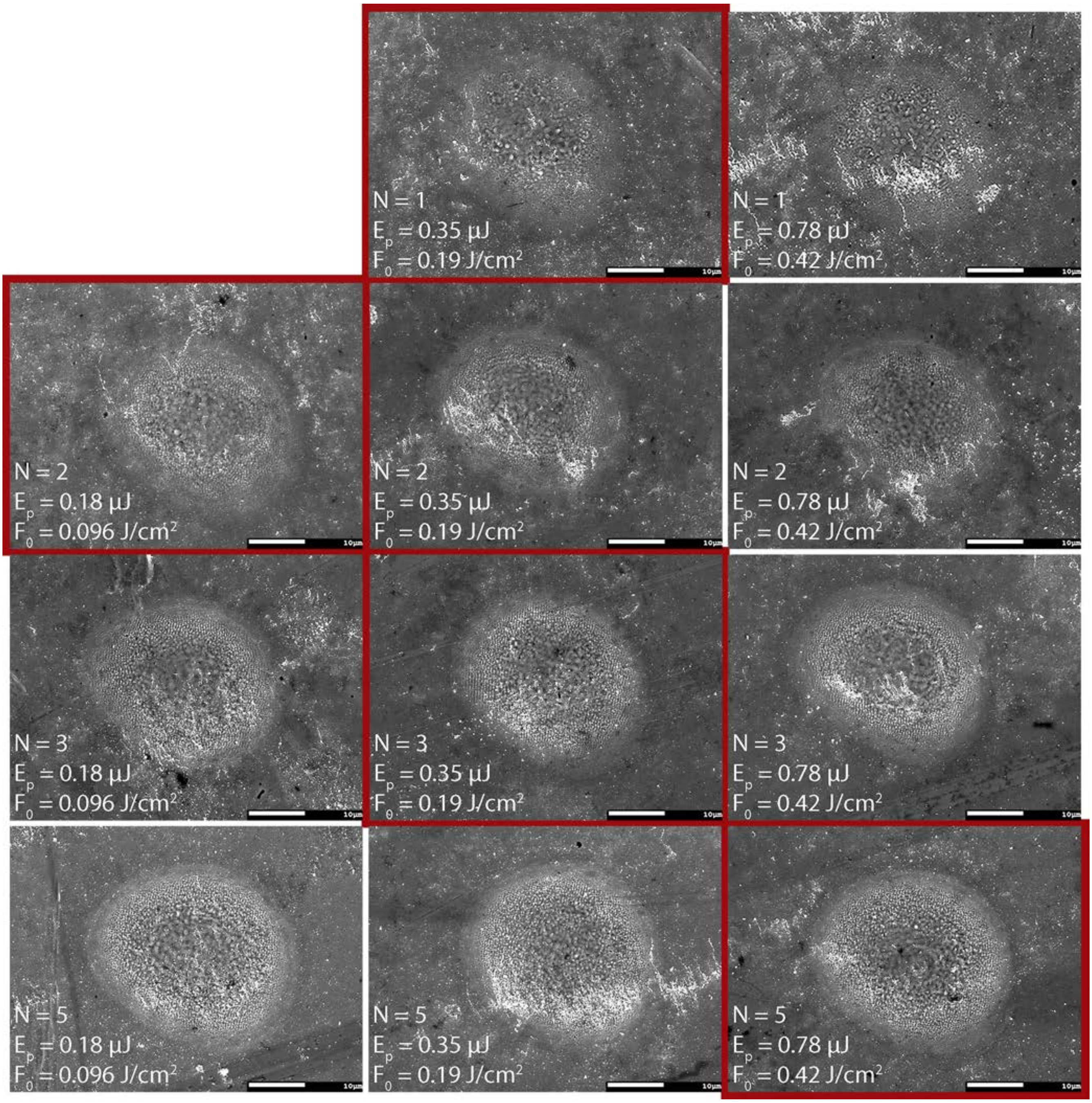

Fig. 4 SEM micrographs of craters created in ambient air on stainless steel. The scale bar length is 10 µm. Notice no result was obtained for N =1 pulse at a pulse energy of 0.18 µJ. The red squares around some of the micrographs indicate the conditions for which confocal analyses were performed in Fig. 6. Here, the upper edge of the micrographs corresponds to the area that was closest to the top of the custom set-up (see Fig. 2) during ablation.

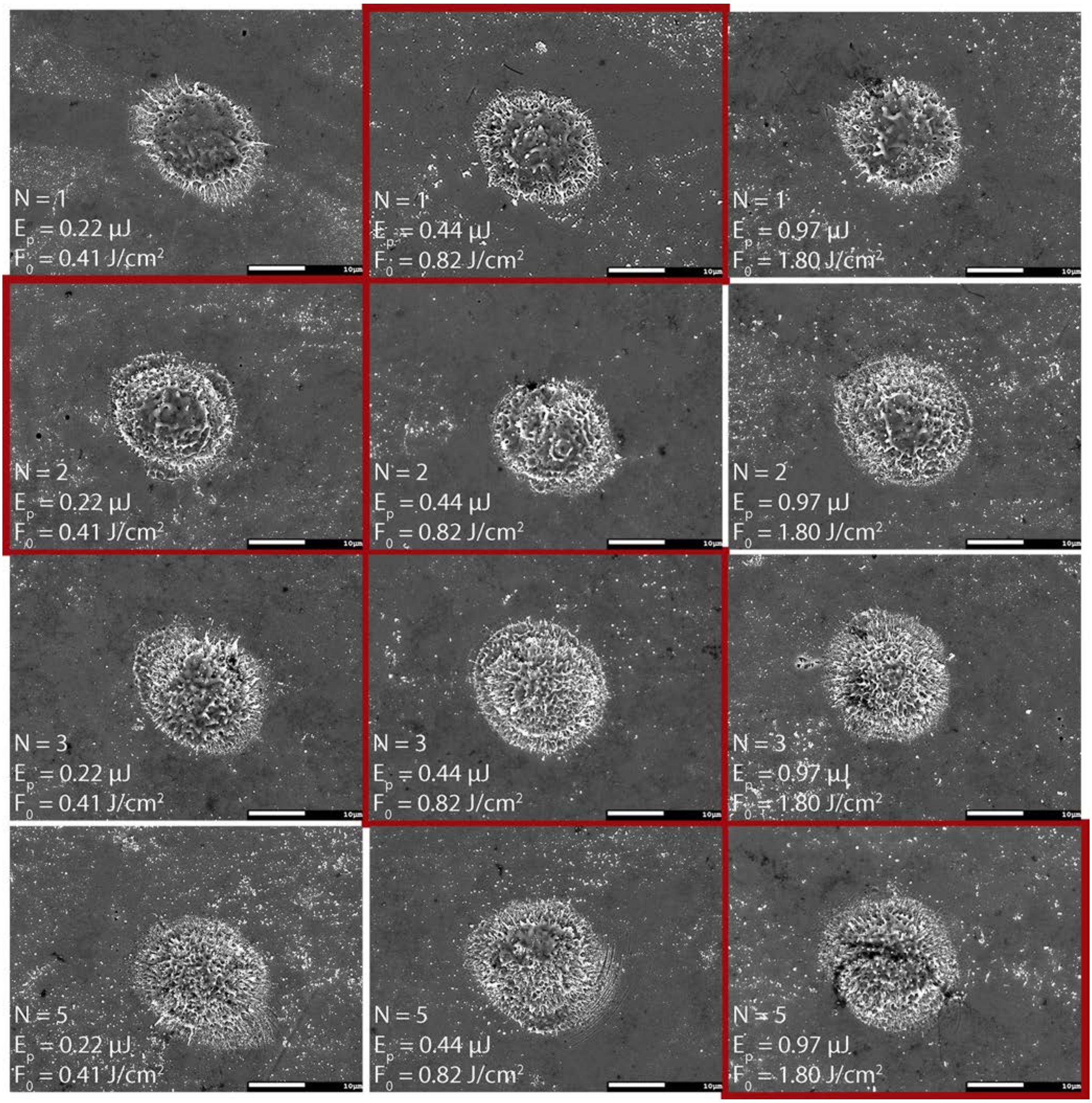

Fig. 5 SEM micrographs of craters under a 2 mm distilled water layer on stainless steel. The scale bar length is 10 µm. The red squares around some of the micrographs indicate the conditions for which confocal analyses were performed in Fig. 7. Here, the upper edge of the micrographs corresponds to the area that was closest to the top of the custom set-up (see Fig. 2) during ablation..

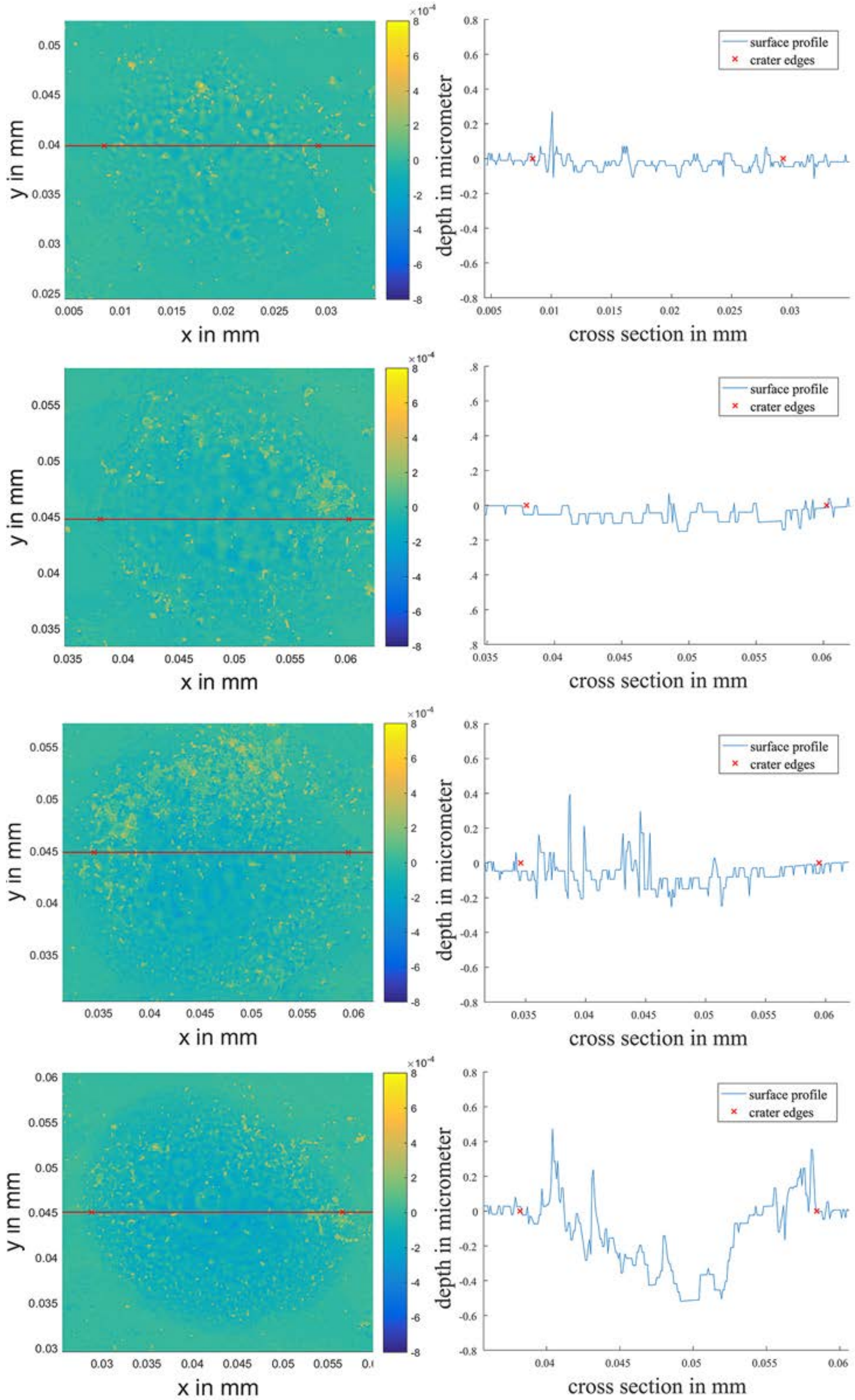

Fig. 6 CLSM images, top view (left) and cross-sections (right) along the red line in the left images, of ablated craters produced in ambient air. Crosses denote manually selected edges of the craters. Ablation conditions from top to bottom: E_p= 0.35 µJ N = 1, F_0 = 0.19 J/cm^2, E_p=0.18 µJ N=2 F_0 = 0.096 J/cm^2, E_p= 0.35 µJ N= 3 F_0 = 0.19 J/cm^2 and E_p= 0.78 µJ N= 5 F_0 = 0.42 J/cm^2. The scale bar is set to millimeters in every graph. The z = 0 line is the reference height of the average unablated sample surface. Here, the upper edge of the micrographs corresponds to the area that was closest to the top of the custom set-up (see Fig. 2) during ablation.

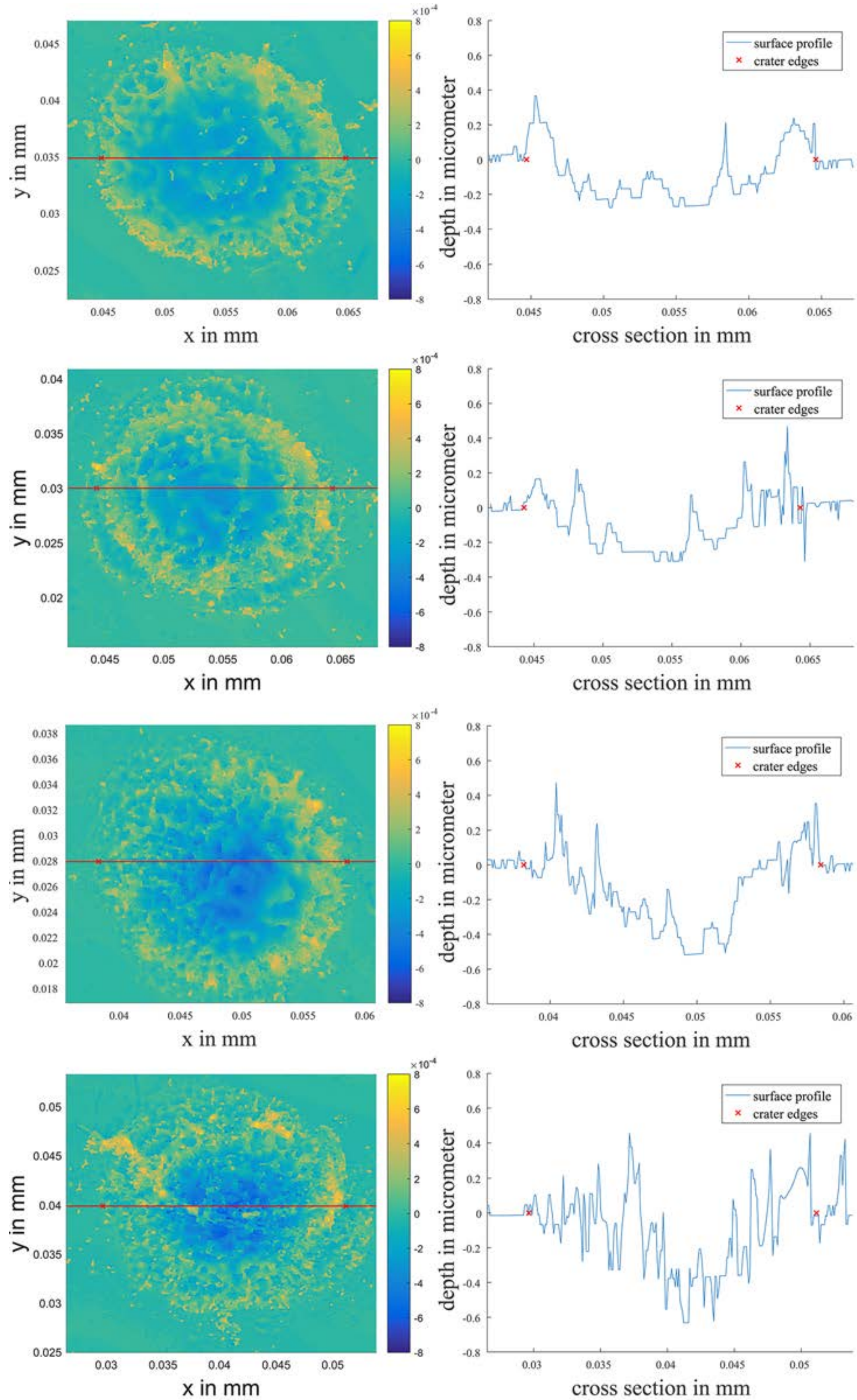

Fig. 7 CLSM images, top view (left) and cross-sections (right) along the red line in the left images, of ablated craters produced under a 2 mm distilled water layer. Crosses denote manually selected edges of the craters. Ablation conditions from top to bottom: E_p= 0.44 µJ N = 1 F_0 = 0.82 J/cm^2, E_p= 0.22 µJ N=2 F_0 = 0.41 J/cm^2, E_p= 0.44 µJ N=3 F_0 = 0.82 J/cm^2 and E_p= 0.97 µJ N=5 F_0 = 1.80 J/cm^2. Scale bar is set to millimeters in every graph. The z = 0 line is the reference height of the average unablated sample surface. Here, the upper edge of the micrographs corresponds to the area that was closest to the top of the custom set-up (see Fig. 2) during ablation.

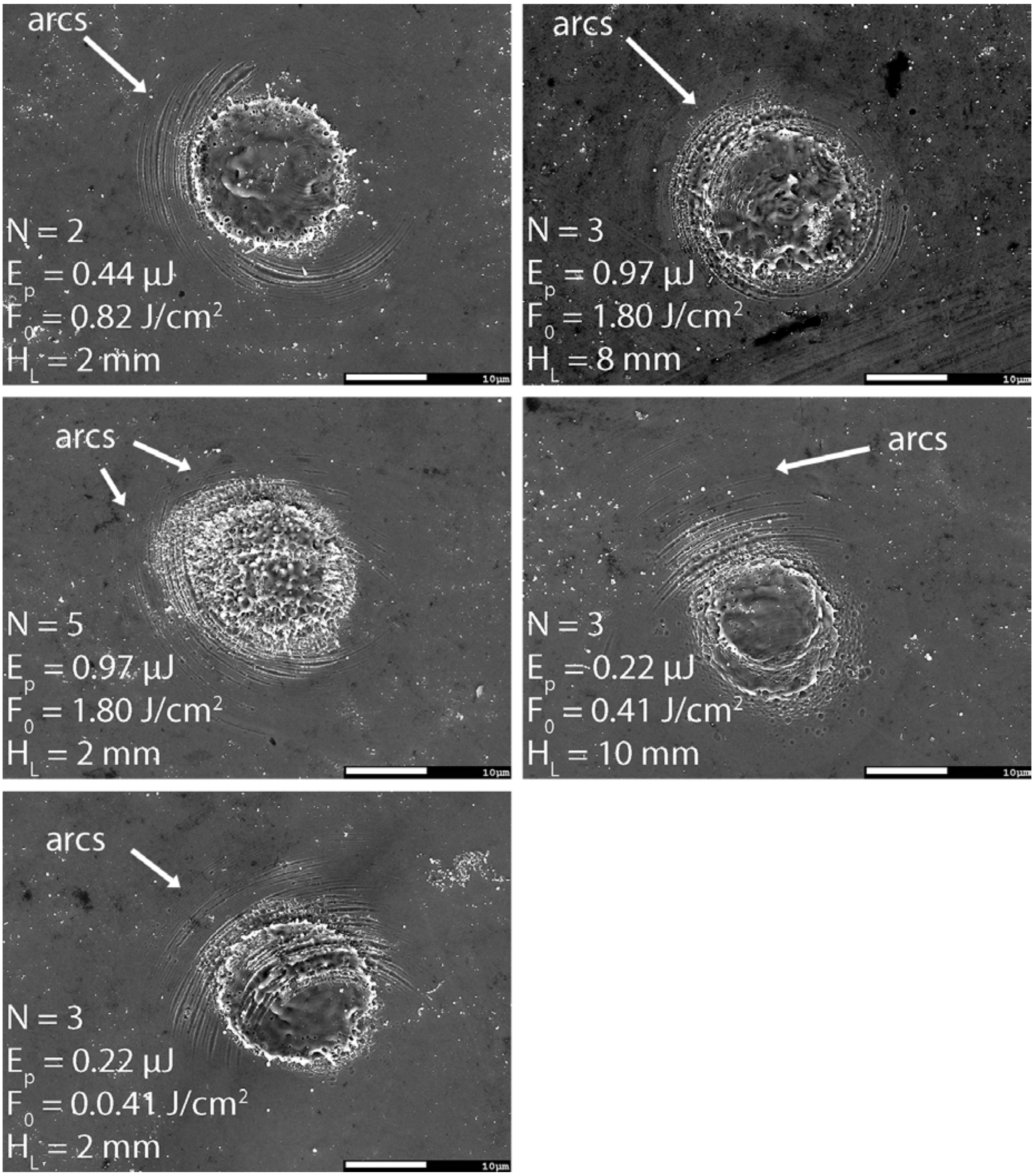

Fig. 8 Arc like structures found around ablated craters when laser processing under a liquid layer, top left: similar structures oriented in a half circle. Top right: full circle structures . Middle left: Intersecting circular arcs with two different radii centers. Middle right: circle parts extending well outside the diameter of the ablation crater. Bottom left: Circle arcs mostly confined to ablated crater. Here, the upper edge of the micrographs corresponds to the area that was closest to the top of the custom set-up (see Fig. 2) during ablation.

4.4 AFM measurements

To further analyze the arc-like structures, an AFM measurement was performed on the crater shown in the top left corner of Fig. 8 and is shown in Fig. 9 and Fig. 10. The zoomed in picture in Fig. 10 reveals that the average arc periodicity for the arcs occurring on the left side of the crater over a total of 13 peak-to-peak distances (denoted by the red dots in the lower picture in Fig. 10) is 500 nm or 0.97λ. Peak to trench distances vary between 420 nm and 3111 nm. The circle drawn in the top image of Fig. 10 indicates that although the arcs seem circular, they are in fact elliptic in nature with focal points which do not coincide with the center of the ablation crater.

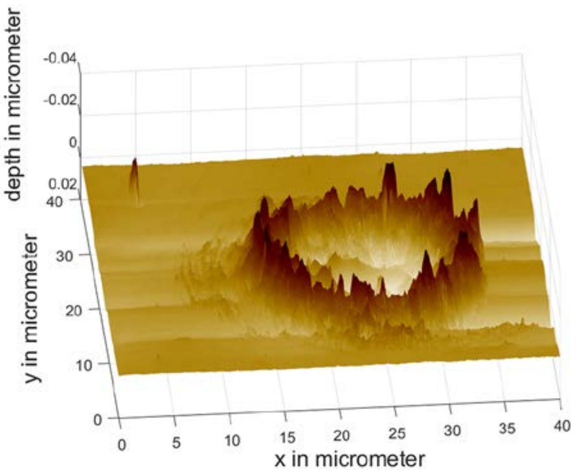

Fig. 9 Isometric view of the AFM measurement of the top left crater in Fig. 8. The peak in the top left is a dust speckle and may be disregarded.

4.5 Arcs in relation to LSFL and occurrence

The periodicity of the arcs indicates that the arcs have the same spatial order of magnitude as Low Spatial Frequency Laser Induced Periodic Surface Structures (LSFL). For metals, the orientation of LFSL are strongly linked to the polarization of the laser light. That is, their orientation is either parallel or perpendicular to the polarization direction depending on the material [22]. As shown in Fig. 8, the observed arcs are circular in nature. As the laser beam was linearly polarized, it seems unlikely that the observed arc-like structures are, in fact, LSFL or any LIPPS for that matter.

The occurrence of the arcs seems to increase with the number of laser pulses. Interestingly, the majority (and most prominent) of the arcs were obtained under a 2 mm water layer: out of the 23 observed craters with arcs on or near them, 17 of them were obtained under a 2 mm water layer. It is known that a liquid environment entraps the plasma produced after laser ablation, which then cools down to form a bubble which implodes on the ablated surface in an oscillatory fashion [23]. As these phenomena typically take place in the nanosecond and microsecond time range respectively [24] and the time between consecutive laser pulses is set to 1 millisecond, it is not likely that the plasma or the imploding cavitation bubble directly contribute to the formation of arcs. It is however, very well possible that bubbles other than the imploding cavity bubble on the surface of the sample may occur in the liquid after some time [25]. The latter bubbles may very well continue to exist in the liquid for more than 1 millisecond [25]. The increase in arc occurrence for a 2 mm liquid layer thickness suggests arc formation dependence on the liquid layer size. The reason behind this dependence is yet unknown but will be investigated in future work.

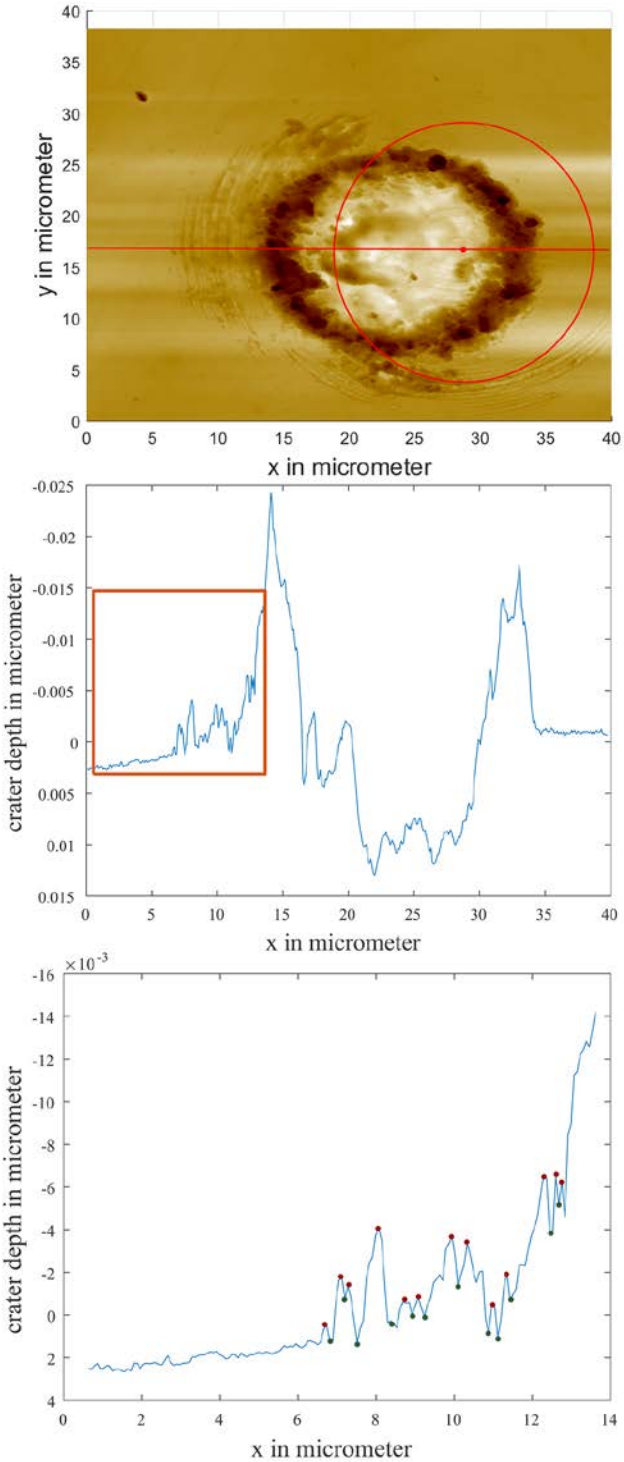

Fig. 10 AFM data of the top left crater of Fig. 8. Upper graph: top view of crater with circle to estimate arc circularity. Middle graph: crater cross section(along the red line in the top graph). Bottom graph: zoomed graph of red boxed area in the middle graph. Red dots denote the estimated ripple peaks, green dots denote trenches. The z = 0 line refers to the average sample surface height.

4.6 Arc formation mechanism

During the single pulse femtosecond pulsed ablation of silicon under a water layer [21], similar arc like structures as the one reported in this paper were described. The difference with arcs described in this work are the facts that the arcs were not observed when processing in ambient air and only appear after 2 or more laser pulses under water. As was previously discussed, bubbles with a lifetime of more than a millisecond may well exist within the liquid during the ablation process [25]. Given that concentric ring creation in silicon is bubble based, perhaps the bubbles in the liquid layer occasionally obstruct the beam path, creating the arc like structures presented in our work. Further work is required to confirm this theory

Several physical phenomena could induce the formation of arcs on the surface. For example, arc features seemingly akin to the ones described in this paper were observed during femtosecond pulsed ablation of glass [26]. Pulse interaction with the shockwave generated by a pre-pulse is concluded to be the cause of the created structures. In principal, the free surface of the custom set-up discussed in this paper may cause reflections of pressure waves to hit the sample. Given the velocity of sound in water [27] and the typical liquid layer thicknesses in our experiments, these reflections could imping the surface of the sample a few microseconds after they started from the surface. For the mechanism described in the ablation of glass to be relevant for the observed arc structures under a water film though, the reflected waves would have to persist for 1 millisecond. Research on optical breakdown of distilled water shows shockwaves created during this process have a lifetime in the order of nanoseconds [28]. Given the similarities between the optical breakdown of water and the under liquid laser ablation process [24], it is unlikely that the shockwaves in the under liquid laser ablation process persist for 1 millisecond.

5. Conclusions

Picosecond pulsed laser ablation under a precisely defined set of distilled water layer thickness was performed for 1, 2, 3 and 5 consecutive pulses and for three different pulse energy levels. Craters for pulse energies of 0.18, 0.35 and 0.78 µJ for ablation in ambient air and 0.22, 0.44 and 0.97 for ablation under a water layer were created using laser light of 515 nanometer. A clear difference in crater morphology was observed between ambient water and ambient air ablated craters: craters created in ambient distilled water were deeper, had a smaller diameter and contained more spike like structures than the in air ablated craters. A satisfactory explanation for the diameter difference was not found, although non-linear optical effects were excluded as a possible cause. The number of craters shot was rather small, creating large uncertainties in the crater diameter analysis. Arc-like surface structures near the ablated craters were observed for multi-pulse under water ablated regions. It does not seem likely that these arcs are laser-induced Periodic Surface Structures (lIPSS). Instead, they are likely caused by bubbles created at some point in the ablation process and which ultimately end up in the path of the laser beam.

Acknowledgments

The research reported in this paper was carried out within the framework of the European INTERREG V A project “Safe and Amplified Industrial Laser Processing” (SailPro), as part of the “RegiOnal Collaboration on Key Enabling Technologies” (ROCKET).

Additionally, dr. Rob Bosman is acknowledged for operating the AFM and for assisting in the AFM data analysis.

References

[1] R. R. Behera, M. R. Sankar, J. Swaminathan, I. Kumar, A. K. Sharma, and A. Khare: Int. J. Adv. Manuf. Technol., 85, (2016) 1969.

[2] V. Tangwarodomnukun and H. Y. Chen: Mater. Manuf. Process., 30, (2015) 685.

[3] N. Iwatani, H. D. Doan, and K. Fushinobu: Int. J. Heat Mass Transf., 71, (2014) 515.

[4] R. Karimzadeh, J. Z. Anvari, and N. Mansour: Appl. Phys. A, 94, (2009) 949.

[5] N. Krstulović, S. Shannon, R. Stefanuik, and C. Fanara: Int. J. Adv. Manuf. Technol., 69, (2013) 1765.

[6] S. Zhu, Y. F. Lu, and M. H. Hong: Appl. Phys. Lett., 79, (2001) 1396.

[7] H. Liu, F. Chen, X. Wang, Q. Yang, H. Bian, J. Si, and X. Hou: Thin Solid Films, 518, (2010) 5188.

[8] N. Ali, S. Bashir, Umm-I-Kalsoom, M. Akram, and K. Mahmood: Appl. Surf. Sci., 270, (2013) 49.

[9] S. Besner, J. Y. Degorce, A. V. Kabashin, and M. Meunier: Appl. Surf. Sci., 247, (2005) 163.

[10] J. M. Liu: Opt. Lett., 7, (1982) 196.

[11] Y. Jee, M. F. Becker, and R. M. Walser: J. Opt. Soc. Am. B, 5, (1988) 648.

[12] J. Bonse, J. M. Wrobel, J. Krüger, and W. Kautek: Appl. Phys. A Mater. Sci. Process., 72, (2001) 89.

[13] J. Bonse, S. Baudach, J. Krüger, W. Kautek, and M. Lenzner: Appl. Phys. A Mater. Sci. Process., 74, (2002) 19.

[14] T. J. Y. Derrien, R. Koter, J. Krüger, S. Höhm, A. Rosenfeld, and J. Bonse: J. Appl. Phys., 116, (2014).

[15] M. J. Weber: *Handbook of Optical Materials* (CRC Press, 2003).

[16] I. H. Malitson: J. Opt. Soc. Am., 55, (1965) 1205.

[17] R. Kitamura, L. Pilon, and M. Jonasz: Appl. Opt., 46, (2007) 8118.

[18] E. D. Palik: *Handbook of Optical Constants of Solids* (Academic Press, 1997).

[19] A. Menéndez-Manjón, P. Wagener, and S. Barcikowski: J. Phys. Chem. C, 115, (2011) 5108.

[20] P. Lickschat, A. Demba, and S. Weissmantel: Appl. Phys. A, 123, (2017) 137.

[21] G. Daminelli, J. Krüger, and W. Kautek: Thin Solid Films, 467, (2004) 334.

[22] J. Bonse, S. Höhm, S. Kirner, A. Rosenfeld, and J. Krüger: IEEE J. Quantum Electron., 23, (2017).

[23] A. De Bonis, M. Sansone, L. D’Alessio, A. Galasso, A. Santagata, and R. Teghil: J. Phys. D. Appl. Phys., 46, (2013).

[24] M. Dell’Aglio, R. Gaudiuso, O. De Pascale, and A. De Giacomo: Appl. Surf. Sci., 348, (2015) 4.

[25] M. Kalus, N. Bärsch, R. Streubel, E. Gökce, S.

Barcikowski, and B. Gökce: Phys. Chem. Chem. Phys., 19, (2017) 7112.
[26] A. Heins and C. Guo: J. Appl. Phys., 113, (2013).
[27] A. H. Smith and A. W. Lawson: J. Chem. Phys., 22, (1954) 351.
[28] A. Vogel, S. Busch, and U. Parlitz: J. Acoust. Soc. Am., 100, (1996) 148.

(Received: June 24, 2018, Accepted: April 3, 2019)